

Research Paper

Circulating Magnetic Microbubbles for Localized Real-Time Control of Drug Delivery by Ultrasonography-Guided Magnetic Targeting and Ultrasound

Beata Chertok^{1, 2}✉ and Robert Langer^{3, 4, 5, 6}

1. Department of Pharmaceutical Sciences, College of Pharmacy, University of Michigan, Ann Arbor, MI 48109, United States;
2. Department of Biomedical Engineering, College of Engineering, University of Michigan, Ann Arbor, MI, United States;
3. Department of Chemical Engineering, MIT, Cambridge, MA 02139, USA;
4. David H Koch Institute for Integrative Cancer Research, MIT, Cambridge, MA 02139, USA;
5. Institute for Medical Engineering & Science, MIT, Cambridge, MA 02139, USA;
6. Harvard-MIT Division of Health Sciences & Technology, Cambridge, MA 02139, USA.

✉ Corresponding author: beata@umich.edu; Department of Pharmaceutical Sciences, College of Pharmacy, University of Michigan, Ann Arbor, MI 48109, United States

© Ivyspring International Publisher. This is an open access article distributed under the terms of the Creative Commons Attribution (CC BY-NC) license (<https://creativecommons.org/licenses/by-nc/4.0/>). See <http://ivyspring.com/terms> for full terms and conditions.

Received: 2017.04.27; Accepted: 2017.10.03; Published: 2018.01.01

Abstract

Image-guided and target-selective modulation of drug delivery by external physical triggers at the site of pathology has the potential to enable tailored control of drug targeting. Magnetic microbubbles that are responsive to magnetic and acoustic modulation and visible to ultrasonography have been proposed as a means to realize this drug targeting strategy. To comply with this strategy *in vivo*, magnetic microbubbles must circulate systemically and evade deposition in pulmonary capillaries, while also preserving magnetic and acoustic activities in circulation over time. Unfortunately, challenges in fabricating magnetic microbubbles with such characteristics have limited progress in this field. In this report, we develop magnetic microbubbles (MagMB) that display strong magnetic and acoustic activities, while also preserving the ability to circulate systemically and evade pulmonary entrapment.

Methods: We systematically evaluated the characteristics of MagMB including their pharmacokinetics, biodistribution, visibility to ultrasonography and amenability to magneto-acoustic modulation in tumor-bearing mice. We further assessed the applicability of MagMB for ultrasonography-guided control of drug targeting.

Results: Following intravenous injection, MagMB exhibited a 17- to 90-fold lower pulmonary entrapment compared to previously reported magnetic microbubbles and mimicked circulation persistence of the clinically utilized Definity microbubbles (>10 min). In addition, MagMB could be accumulated in tumor vasculature by magnetic targeting, monitored by ultrasonography and collapsed by focused ultrasound on demand to activate drug deposition at the target. Furthermore, drug delivery to target tumors could be enhanced by adjusting the magneto-acoustic modulation based on ultrasonographic monitoring of MagMB in real-time.

Conclusions: Circulating MagMB in conjunction with ultrasonography-guided magneto-acoustic modulation may provide a strategy for tailored minimally-invasive control over drug delivery to target tissues.

Key words: theranostics, magnetic microbubbles, lung evading microparticles, image-guided drug delivery, remote-controlled drug delivery.

Introduction

Efficient systemic drug therapy for cancer and other intractable diseases requires delivery of therapeutically effective drug concentrations to the site of pathology at safe systemic doses. A wide variety of drug carriers have been designed to target diseased tissues by leveraging cell-specific ligands or tumor vascular abnormalities [1]. However, the stochastic nature of these approaches and the high heterogeneity of pathologies, particularly in cancer, compromise attainment of desired drug levels at the target [1, 2].

An emerging therapeutic strategy of theranostics that combines therapeutic and diagnostic components in a single system has the potential to address this challenge by tailoring delivery of therapeutics to each patient's disease state [3, 4]. The key to this strategy is multi-modality drug carriers that can be simultaneously visualized by non-invasive imaging and modulated by external physical triggers to allow localized tuning of drug delivery selectively at the target. Among investigated agents, lipid-shelled microbubbles utilized clinically as contrast agents for diagnostic ultrasonography provide several unique advantages [5]. Lipid-shelled microbubbles are compressible microparticles composed of a gaseous core coated with a thin lipid film. These systemically circulating agents can be visualized by ultrasonography and collapsed by focused ultrasound selectively in target tissues to simultaneously release the drug cargo and promote drug uptake by tissues [6]. However, standard microbubble formulations lack mechanisms for preferential accumulation in target tissues, rendering drug delivery by microbubbles and ultrasound largely inefficient [7]. Ligand-based methods have been explored to target microbubbles to specific sites [8], but paucity of tissue-specific biomarkers and immunogenicity of targeting ligands limit their potential for drug delivery [1, 7-9].

As an alternative, a large body of research in recent years has focused on the development of magnetic microbubbles [7, 10, 11]. Magnetic microbubbles are multi-scale composites of microbubbles and superparamagnetic iron oxide nanoparticles - agents that endow the microbubbles with magnetic responsiveness. Because magnetic microbubbles possess dual sensitivity to ultrasound and magnetic fields, they can, in principle, combine the advantages of both traditional microbubbles and magnetic drug carriers. Magnetic microbubbles have been envisioned to be concentrated in target tumor vasculature by magnetic fields, monitored by

ultrasonography to ascertain delivery and activated by ultrasound to facilitate drug release and extravasation [12]. Because modulation by magnetic fields and ultrasound can be tailored on demand based on ultrasonography information, this multi-modality targeting paradigm could provide a means to control drug doses delivered to the target.

However, formulating magnetic microbubbles for *in vivo* magneto-acoustic drug delivery remains a considerable challenge. Magnetic microbubbles must display high magnetic and acoustic sensitivities, while also preserving the ability to circulate systemically and access the vasculature of target tissues. Unfortunately, microbubble designs that maximize their magnetic activity also impose structural changes that compromise the microbubbles' acoustic properties and circulation stability. [11, 13, 14] To obtain microbubbles with high magnetic responsiveness, iron oxide nanoparticles have been incorporated into the shell of polymer- and lipid-shelled microbubbles, encapsulated in oil-layers of acoustically active lipospheres or attached to the microbubble's surface using avidin/streptavidin-biotin linkers. [11, 15-19] However, integration of rigid nanoparticles into the microbubble's shell stiffens the microbubbles, reducing their sensitivity to ultrasound, [11, 13, 20] while decoration of the microbubble surface with immunogenic ligands leads to complement activation and surface destabilization by complement components [21]. Both the surface destabilization and the stiffening effects increase the undesirable propensity for microbubble entrapment in lung capillaries, [22, 23] leading to first-pass pulmonary clearance of a significant fraction of the dose (17-90%) [11, 14, 18, 24]. Pulmonary entrapment not only prevents the microparticles from reaching the vasculature of peripheral target tumors, but it also poses risks of vascular occlusion and life-threatening thromboembolic toxicity [25]. Clinically used lipid-shelled microbubbles (e.g., Definity) successfully evade entrapment in the lungs and remain in circulation for 5-10 min, providing sufficient vascular exposure for imaging or modulation by external triggers [26, 27]. However, emulating this behavior with multi-scale nanoparticle-carrying magnetic microbubbles remains a considerable challenge.

Here, we develop magnetic microbubbles that mimic the *in vivo* behavior of clinically-utilized lipid-shelled microbubbles (e.g., Definity), while also displaying sufficient magnetic and acoustic sensitivities for magneto-acoustic modulation. The advantageous *in vivo* behavior of Definity-like

microbubbles has been ascribed to their inherent compressibility and surface protection by flexible hydrophilic polymers, termed stealth coatings [5, 26]. We sought to develop magnetic microbubbles with similar attributes. It is known that fabrication of nanoparticle-microbubble composites by attaching nanoparticles to the microbubble's surface can preserve the original microbubble's compressibility [28]. It is also known that heparin, a clinically utilized non-immunogenic anionic polysaccharide, can impart stealth properties to the drug carrier's surface. [29] We considered that attaching heparin-functionalized iron oxide nanoparticles to the surface of lipid-shelled microbubbles could preserve the compressibility of the microbubbles, while also providing their surface with stealth heparin coating. To realize these materials, we developed a methodology based on complexation of heparin with protamine, an arginine-rich cationic polypeptide that is clinically used as heparin's antidote because of its remarkably high affinity ($K_{eq} = 1-20 \times 10^7 \text{ M}^{-1}$) for heparin [30]. By coupling heparinized magnetic nanoparticles to the protamine-functionalized microbubble surface, we fabricated circulation-stable magnetic microbubbles (MagMB) with strong magnetic and acoustic activities. We demonstrate that MagMB circulated systemically, evaded lung entrapment, and could be magnetically retained in tumor vasculature, monitored by ultrasonography and collapsed by ultrasound on demand. We further demonstrate that MagMB could be leveraged to enhance drug delivery to target tumors by real-time adjustment of magneto-acoustic drug targeting based on ultrasonographic monitoring of the carriers.

Materials and Methods

Materials

Lipids including 1,2-distearoyl-*sn*-glycero-3-phosphocholine (DSPC), 1,2-distearoyl-*sn*-glycero-3-phosphoethanolamine-N-[methoxy(polyethylene glycol)-2000] (DSPE-mPEG(2kDa)) and 1,2-distearoyl-*sn*-glycero-3-phosphoethanolamine-N [maleimide (polyethylene glycol)-2000] (ammonium salt) (DSPE-PEG(2kDa)-MAL) were obtained from Avanti Polar Lipids and used without further purification. Hetero-bifunctional cross-linker N-Succinimidyl 3-[2-pyridyldithio]-propionate (SPDP) was obtained from Pierce.

Synthesis of PI-PEG-Prot conjugate

Protamine (5 mg/mL in 100 mM phosphate buffer, pH 7.4) was reacted with a five-fold molar excess of SPDP (dissolved in dimethyl sulfoxide (DMSO)) for 2 h at room temperature. The coupling was quantified with pyridine-2-thione

spectrophotometric assay, calibrated with free pyridine-2-thione in the range of 20-100 μM . The Protamine-PDP product was then reacted with the reducing agent Tris(2-carboxyethyl) phosphine hydrochloride (TCEP-HCL, 50mM) for 2 h to obtain thiolated protamine (Protamine-SH). The sulfhydryl content of the activated Protamine-SH was quantified by Ellman assay, using a well-established procedure [31]. To produce the conjugate (PI-PEG-Prot), Protamine-SH was incubated with DSPE-PEG(2kDa)-MAL (1.5:1 molar ratio, 100 mM phosphate buffer, pH 7.4) at room temperature overnight. Conjugation was confirmed by MALDI-TOF (MicroFlex MALDI-TOF, Bruker) mass spectroscopic analysis (m/z : ~ 7400 for DSPE-PEG(2 kDa)-Protamine).

Preparation of MagMB

Protamine-bearing microbubbles (MB-Prot), comprising octafluoropropane (C_3F_8 , Synquest lab, FL) gas core and phospholipids/ PI-PEG-Prot shell, were prepared by a high-shear emulsification method [32, 33]. The composition of the microbubble formulation mixture was DSPC: DSPE-PEG(2kDa): PI-PEG-Prot (82:18-x:x, mol%), where x is a mol% of PI-PEG-Prot conjugate. The microbubbles were purified by several flotation (300 rcf)/ redispersion cycles to remove the unincorporated lipids. Protamine incorporation into microbubbles was confirmed by the Bicinchoninic acid protein assay (BCA, Pierce). Microbubbles were quantified using the Coulter Counter (Beckman).

Iron oxide nanoparticles coated with heparin were obtained from Chemicell (Germany). The heparinized nanoparticles (MNPh) exhibited a multi-crystalline core, hydrodynamic diameter of $\sim 122 \text{ nm}$ and ζ - potential of -33 mV , as previously described [34, 35]. Nanoparticle preparations were quantified with Inductively Coupled Plasma Optical Emission Spectrometry (ICP-OES) [36].

Magnetic microbubbles (MagMB) were prepared by mixing the suspension of protamine-functionalized microbubbles (MB-Prot) with the suspension of the heparinized nanoparticles (MNPh), followed by two purification steps. In the first step, a combination of gravity separation and centrifugation was used to remove large microbubbles and non-attached nanoparticles [37, 38]. The microbubble suspension was first left to stand for 5 min at room temperature to allow flotation of large microbubbles ($>8 \mu\text{m}$). [38] The remaining suspension (infranate) was decanted and centrifuged (300 rcf) to collect all remaining microbubbles into a cake layer. The respective infranate was discarded to remove non-attached nanoparticles. In the second step, the cake layer was reconstituted with PBS and placed on a magnetic

separator. The fraction that migrated to the magnet (MagMB) was collected and the non-magnetic fraction discarded. Representative microbubble size distributions and counts obtained during the purification procedure are provided in Figure S3. Typical yields of purified MagMB relative to the initial counts of MB-Prot were 30-35%.

Characterization of MagMB

Morphological characterization

Morphological characterization of MagMB was conducted using bright field optical microscopy (Axiovert 200M, Zeiss), transmission electron microscopy (TEM, JEOL JEM 200CX) and cryoTEM (Jeol 2100 FEG TEM, equipped with the Single Tilt Liquid Nitrogen Cryo-Transfer Holder, Gatan). For optical microscopy, samples of aqueous microbubble suspension were spotted on a glass slide, coverslipped and imaged through the coverslip using 20x (air) and 100x (oil) objectives. For TEM, samples of aqueous microbubble suspension were spotted onto a holey carbon-film coated grid (CF200-Cu, EMS) and allowed to dry at room temperature. For cryoTEM, samples of aqueous microbubble suspension were spotted onto a holey carbon-film coated grid (Quantifoil R5/20) and immersion-frozen with the semi-automatic cryo-plunger (CryoPlunge3, Gatan). The size distribution of MagMB was analyzed with Multisizer 3 Coulter Counter (Beckman Coulter). The zeta potential was analyzed by phase analysis light scattering using ZetaPALS (Brookhaven).

Nanoparticle loading

For quantitative analysis of MNPh loading, MagMB were disrupted by brief sonication and MNPh quantified by ICP-OES as previously described [36]. Amounts of MNPh in microbubble samples were normalized by the microbubble counts.

Magnetic capture assay

The analysis of the magnetic properties of MagMB was conducted with a dynamic flow assay [36]. The microbubble samples were infused at linear flow rates of 0.04-0.7 cm/s through a capillary tubing (ID = 0.58 mm) exposed to a magnetic field. The applied magnetic field was adjusted to 0.9 T (test, grad B = 50 T/m) or 0 T (control). The microbubble counts in the feed and the collector reservoirs were determined by the Coulter Counter (Beckman). The percent of the magnetically captured microbubbles was plotted as a function of the flow rate.

Acoustic destructibility assay

To assess the acoustic destructibility, microbubbles (10^7 /mL) were subjected to 1 MHz

sinusoidal tone-bursts of acoustic insonation for 0-80 s with the following parameters: pulse duration (PD) – 33 μ s, pulse repetition frequency (PRF) – 3 kHz and peak negative pressure (PNP) – 0.22 MPa. Similar insonation conditions have been previously utilized to enhance drug delivery by ultrasound-mediated microbubble destruction. [39-42] The acoustic setup (Figure 4, A1) comprised a single-element 1 MHz ultrasound transducer (25 mm aperture, 55 mm focal length: Precision Acoustics, UK) mounted in a water tank and driven by a wavefunction generator (Tektronix) and a 50 dB radio-frequency amplifier (ENI). [32] The sample chamber (2 mL) sealed at the top and the bottom with the Mylar membrane was pre-filled with degassed PBS. Microbubble samples were injected through a side port and re-dispersed in PBS. The sample chamber was submerged in the water tank and secured at the focal length from the face of the transducer. The acoustic pressure at the sample plane was calibrated with a 0.5 mm needle hydrophone (Precision Acoustics, UK) connected to a PC oscilloscope (PicoScope 4224, Pico Technology). Following acoustic insonation (0-80 s), the residual microbubble counts were quantified with the Coulter Counter. Post insonation counts were normalized by the 0 s insonation counts (defined as 100%). To determine the microbubble half-life under acoustic insonation, an exponential decay model $y = Ae^{-x/t}$ was fitted to the data sets of normalized post-insonation counts over time using OriginPro9.

Serum stability

The microbubble composites were tested for serum stability. Purified, nanoparticle-loaded microbubble samples engrafted with MNPh (20 ± 3 fg Fe/ μ m²) were re-dispersed in either fetal bovine serum (FBS, 50%) or PBS. Following incubation at room temperature for 30 min, the microbubbles were collected by flotation, counted, disrupted by brief sonication and analyzed for content of MNPh as described above.

In vivo studies

All animal procedures were approved by the MIT and the University of Michigan Institutional Committees on Animal Care.

Establishment of subcutaneous tumors in mice

Murine LL/2 Lewis lung carcinoma cells (ATCC: CRL-1642) were grown as monolayers in DMEM media supplemented with 10% fetal bovine serum. For implantation, the cells were harvested by trypsinization (0.25% Trypsin-EDTA, Gibco) and resuspended in sterile PBS at 2×10^7 cell / mL. Tumors were established in the rear flank of 6- to 8-week-old SCID mice (SHO, Charles River) by

subcutaneous injection of cell suspension (50 μL , 1×10^6 cells). Tumors were allowed to grow for 7-14 days to a volume of $\sim 500 \mu\text{L}$.

Biodistribution analysis

For biodistribution analysis, the microbubbles were labeled with the near-infrared dye Cy5.5 through incorporation of DSPE-PEG(2kDa)-Cy5.5 (0.1% of lipid composition). Microbubble suspensions (MagMB-Cy5.5, 100 μL , 1×10^9 /kg) were administered to mice intravenously, via catheterized lateral tail-vein. The biodistribution was assessed by the whole-body fluorescence imaging and by *ex vivo* organ analysis. Fluorescence imaging (excitation/emission at 640 nm/720 nm, epi-illumination mode) was conducted using IVIS Spectrum imaging system (Xenogen). Animal organs were harvested, flash-frozen in liquid nitrogen and stored at -80°C until analysis.

In vivo echogenicity and pharmacokinetic analysis by ultrasonography

Real-time image-monitoring of microbubbles was performed with the high-frequency ultrasound imaging system (Vevo 770[®], Visual Sonics) equipped with a 30 MHz linear transducer RMV-707B (Visual Sonics). The transducer had a lateral and axial resolution of 115 μm and 55 μm , respectively, and a focal length of 12.7 mm. The geometric focus of the transducer was aligned with the renal artery. A solid gel standoff of $\sim 5\text{-}7$ mm thickness (Aquaflex ultrasound gel pad, Parker lab) and the ultrasound transmission gel (Aquasonic-100, Parker lab) were used to provide acoustic coupling. The images were acquired over a field of view of 12 mm x 12 mm using 20% transmit power.

The microbubble suspension (100 μL) was administered via the catheterized lateral tail vein by an i.v. bolus injection. The doses of 7.5×10^7 /kg and 1×10^9 /kg were used for analyses of *in vivo* echogenicity and pharmacokinetics, respectively. Similar doses were previously used in diagnostic and therapeutic studies, respectively. [41, 43, 44] Microbubble perfusion through the organ of interest (renal artery) was monitored by sequential acquisition of two-dimensional, fundamental-frequency B-mode scans. For pharmacokinetic monitoring, scans were acquired before, during and post injection at a 30-50 Hz frame rate for the first 60 s and then sequentially at 60 s intervals.

Magneto-acoustic targeting

Targeting setup

Targeting experiments were conducted with an in-house-assembled magneto-acoustic targeting setup

(Figure 6, A1). A DC magnetic field (Figure 6, A3) was generated by a dipole electromagnet (GMW Associates, CA). Acoustic insonation was produced with a 1 MHz, focused ceramic transducer (25 mm diameter, 55 mm focal length) actuated in tone-bursts as described in section "Acoustic destructibility assay". Animals were aligned on a platform with their tumor positioned within the airgap between the magnet poles. The 1 MHz transducer and the 30 MHz imaging probe were aligned orthogonally to the airgap plane and to one another. The geometric focus of the imaging probe (30 MHz) was positioned at the tumor mid-plane (Figure 6, A2 and A4). A solid gel standoff of a ~ 7 mm thickness (Aquaflex ultrasound gel pad, Parker lab) and the ultrasound transmission gel (Aquasonic-100, Parker lab) were used to provide acoustic coupling. Mice were administered with microbubbles via catheterized lateral tail-vein, and microbubble perfusion through the organ of interest (tumor vasculature) was monitored by ultrasonography as described in section "*In vivo* echogenicity and pharmacokinetic analysis by ultrasonography". Each animal received a single 100 μL bolus injection of microbubbles (1×10^9 /kg) during the course of an experiment. The tumors were exposed to the magnetic targeting (field and gradient of 0.9 T and 50 T/m, respectively) and ultrasound insonation (the Ultrasound Targeted Microbubbles Destruction or UTMD protocol: PNP = 0.22 MPa, PRF = 3 kHz, PD = 33 μs).

Study design for testing magneto-acoustic modulation of MagMB

The behavior of MagMB in tumors under magneto-acoustic modulation (magnetic targeting + UTMD) was tested in two groups of mice. Both groups received a single i.v. bolus injection of MagMB (100 μL , 1×10^9 /kg). The test group was exposed to magnetic targeting for 30 min, and thereafter, to UTMD for 50 s at 40 min post microbubble administration. No physical forcefields were applied on the interval of 30-40 min post microbubble administration. The control group was not subjected to physical forcefields. The time-line of treatment administration is depicted in Figure 6, B.

Study design for testing drug delivery

In vivo delivery of a model drug Cy5.5 to tumors using MagMB-Cy5.5 was tested in seven groups of mice. Each group received a single i.v. bolus injection of MagMB-Cy5.5 (100 μL , 1×10^9 /kg) and was subjected to one of the following treatments: (1) (MF-, US-) no magnetic targeting or UTMD, (2) (MF+, US-) magnetic targeting only, (3) (MF-, US+) UTMD only, (4) (MF+, US+) combination of magnetic targeting and

UTMD. For treatments 2-4, magnetic targeting was applied for 1 min or 5 min, immediately followed by UTMD for 50 s at 1 min or 5 min post microbubble administration, respectively. At 120 min post-treatment, the delivery of the model drug (Cy5.5) to tumors was quantified by fluorescence imaging as described in section "Biodistribution analysis". The time-line of treatment administration and drug delivery assessment is depicted in Figure 7, A.

Ex vivo analysis

Quantitative analysis of the microbubble biodistribution was conducted according to our previously reported procedure.[32] Briefly, mouse organs were cryogenically ground with the Geno/Grinder (Spex), extracted with the Glo lysis buffer (Promega), and analyzed for fluorescence intensity using fluorescence spectroscopy (excitation/emission at 640nm/710nm).

Image analysis

Ultrasound imaging

Video intensity ultrasound data were analyzed using custom software developed with the Matlab R2015 software package. To assess kinetics of microbubble transit and microvascular retention, microbubble-dependent contrast enhancement (CE) within the region of interest (ROI) was calculated at image-monitored time points (t) in two steps. First, CE at time t was calculated as a difference between the post-injection image frame at time t and the background signal averaged over 50-100 consecutive pre-injection frames. Then, $CE_{ROI}(t)$ was calculated as the average CE(t) pixel intensity within the ROI drawn to outline the relevant area (the renal artery (RA) or tumor area (T)) on the B-mode scan. $CE_{ROI}(t)$ values were plotted as a function of time to generate time-intensity curves. To allow for averaging of time-intensity curves from different subjects while accounting for variation in image acquisition time points, linear interpolation was applied to the data sets.

The *in vivo* echogenicity of microbubbles was quantified as the peak signal enhancement of the renal artery by microbubbles (7.5×10^7 /kg, 100 μ L, i.v. bolus) normalized by the pre-injection renal artery baseline. The *in vitro* echogenicity was quantified as the signal enhancement generated by suspending microbubbles in PBS (10^6 /mL) normalized by the respective PBS baseline.

Fluorescence *in vivo* imaging

Fluorescence image analysis was conducted with

the Living Image 4.4 software package. The ROI was drawn to outline the relevant area on the whole-body or individual organ scans. Tumor ROI data were offset by blank controls. Tumor ROIs of animals imaged under the same fluorescence conditions as the test mice but not exposed to MagMB-Cy5.5 were used as blank controls.

Statistical analysis

Data are expressed as mean \pm SD unless otherwise specified. Comparisons between 2 groups were made using the unpaired t-test. Means of multiple groups were compared with the 1-way ANOVA, followed by post hoc Tukey's pairwise comparisons. The acoustic destruction data for different microbubble samples were compared through curve fitting analysis. An exponential decay model was first fitted globally to concatenated datasets and then separately to individual data sets of microbubble counts over time. The goodness-of-fit was compared using the extra-sum-of-squares F test. All probability values are 2-sided, and values of $p < 0.05$ were considered statistically significant. Curve fitting and statistical analyses were carried out using OriginPro9 (OriginLab) and SPSS (IBM) software packages.

Results and Discussion

Fabrication and optimization of magnetic microbubbles

To assemble magnetic microbubbles, we developed a two-step methodology (Figure 1, A.a). We first prepared protamine-functionalized microbubbles (MB-Prot, Figure 1, A.a - step i) and then attached heparin-functionalized magnetic nanoparticles (MNPh) to the surface of MB-Prot (Figure 1, A.a - step ii). To prepare MB-Prot, we synthesized an amphiphilic phospholipid-PEG-protamine conjugate (PL-PEG-Prot, Figure 1, A.b). We reasoned that the amphiphilic conjugate would self-insert into the phospholipid microbubble shell and allow protamine to display on the microbubble's surface. Indeed, the PL-PEG-Prot conjugate could be integrated into microbubbles by adding PL-PEG-Prot to the microbubble's lipid formulation. The conjugate-modified microbubbles displayed significantly higher protamine content and a significantly higher zeta potential compared to controls (Figure 1, B-C, $p < 0.001$). These findings confirmed insertion of PL-PEG-Prot into the microbubble's shell and the display of cationic protamine on the microbubble's surface, respectively.

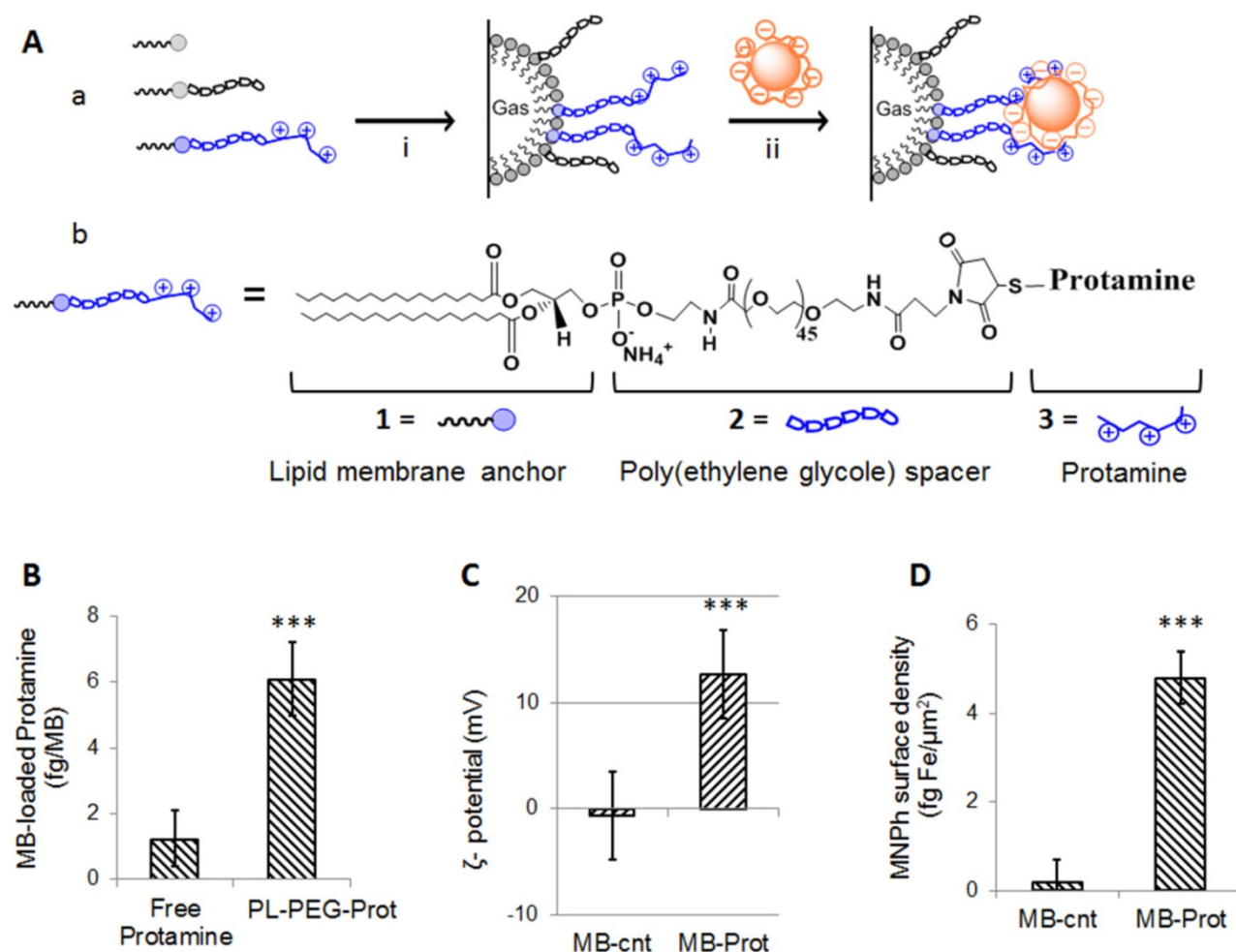


Figure 1. Fabrication of magnetic microbubbles. (A) a. Scheme of the two-step assembly of magnetic microbubbles – step I: preparation of protamine-functionalized microbubbles; step II: coupling of protamine-functionalized microbubbles with heparin-coated iron oxide nanoparticles. (A) b. Structure of PL-PEG-Prot conjugate comprising (1) lipid membrane anchor, (2) poly(ethylene glycol) 2 kDa spacer, and (3) protamine. (B) Analysis of protamine concentrations in microbubble samples incubated with free protamine and PL-PEG-Prot. Data represent mean \pm SD, $n = 4$. (C) Zeta potential of MB-cnt and MB-Prot dispersed in PBS, pH 7.4. Data represent mean \pm SD, $n = 4$. (D) Analysis of MNPh loading in control MB-cnt and protamine-functionalized microbubbles MB-Prot. Data represent mean \pm SD, $n = 4$. Statistical comparisons are based on unpaired t-test. Asterisks denote statistically significant differences: * $p < 0.05$, ** $p < 0.01$, *** $p < 0.001$. MB: microbubbles; MB-Prot: microbubbles functionalized with protamine; MNPh: magnetic nanoparticles coated with heparin; PBS: phosphate buffered saline; PEG: poly(ethylene glycole); PL: phospholipid; Prot: protamine.

Subsequently, we tested the feasibility of attaching heparinized nanoparticles (MNPh) to the surface of protamine-functionalized microbubbles. To assemble nanoparticles-microbubble composites we simply mixed MNPh with MB-Prot. Significantly higher loading of MNPh ($p < 0.001$) was achieved by mixing of MNPh with protamine-functionalized microbubbles than with protamine-free control microbubbles (Figure 1, D). These findings corroborated the viability of heparin-protamine complexation as a means of forming nanoparticles-microbubble composites (MB-Prot/MNPh).

Next, we carried out optimization of composite microbubbles. First, to display heparin as a surface coating on the microbubble's surface we sought to saturate pendant protamine chains of MB-Prot with heparin-carrying nanoparticles. To achieve that, we performed optimization of nanoparticle loading onto

the microbubble's surface by mixing MB-Prot samples (0.22 ± 0.03 fg protamine per μm^2 surface area) with increasing concentrations of MNPh. The amount of nanoparticles attached to the microbubble's surface increased with increasing mixing ratios of MNPh to MB-Prot and reached a plateau at 400 fg Fe/ MB (Figure 2, A1). Notably, the increased nanoparticle loading was mirrored by a corresponding reduction in zeta-potential (Figure 2, A2). The zeta potential of the cationic MB-Prot (12 ± 2 mV) gradually decreased with increasing loading of MNPh and reached electronegative potential (-11 ± 2 mV) for nanoparticle-saturated MB-Prot/MNPh composites. Reversal of zeta potential at saturation reflected successful masking of cationic protamine on the microbubble's surface by anionic heparin-carrying nanoparticles.

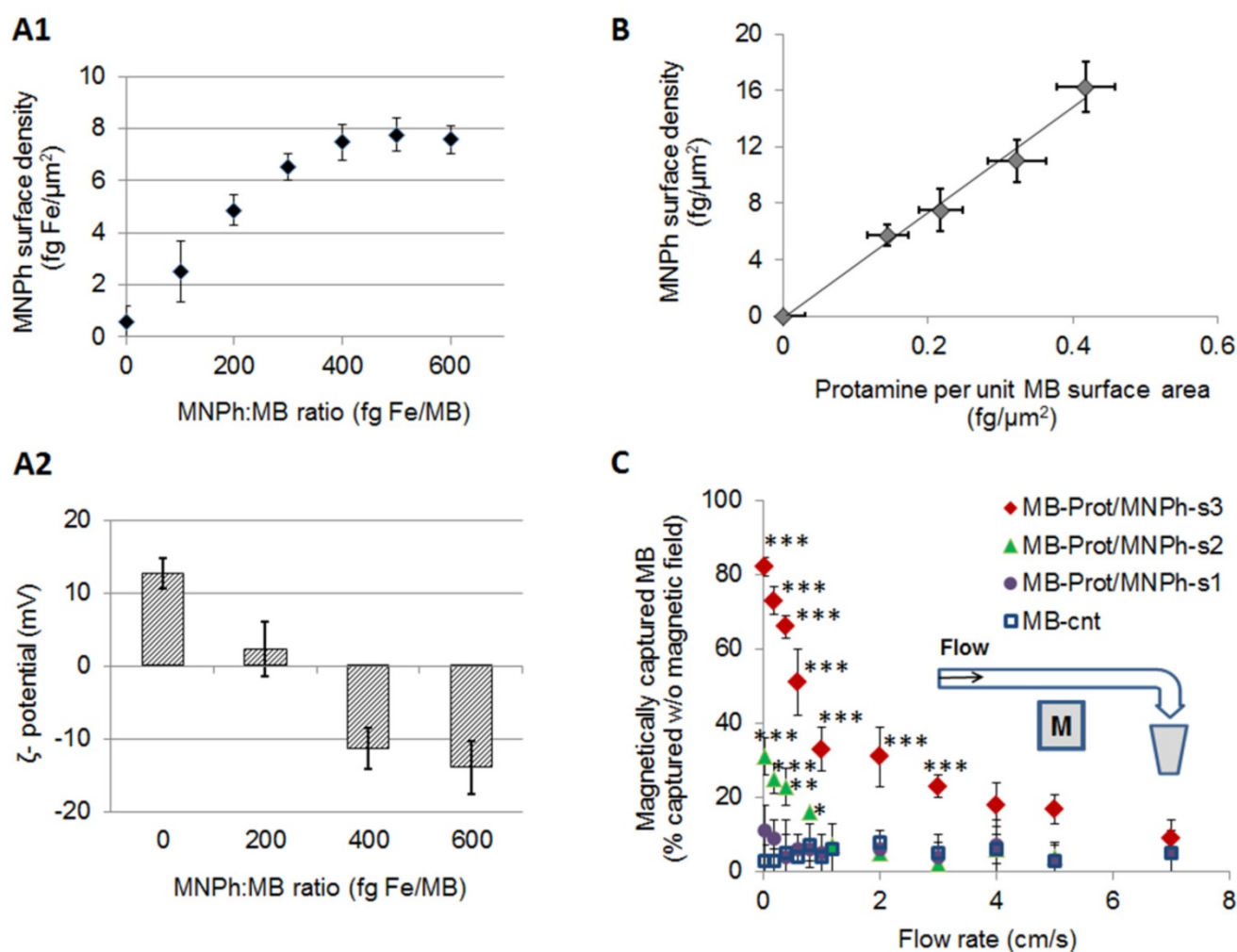


Figure 2. Optimization of surface and magnetic properties of magnetic microbubbles. (A) Dependence of MNPh nanoparticle content (A1) and zeta potential (A2, PBS, pH 7.4) of the nanoparticles-microbubble composites on nanoparticle-to-microbubble incubation ratios. Data represent mean \pm SD, $n = 4$. (B) Dependence of microbubble loading with MNPh nanoparticles on the protamine content of microbubbles MB-Prot. Data were fitted to a linear model, $R^2 = 0.99$, $p = 0.002$. (C). Capture of microbubbles by an applied magnetic field ($B = 0.9$ T, $\text{grad } B = 50$ T/m) under physiological flow conditions. Inset: Schematic depiction of the setup for dynamic magnetic capture assay. Statistical analysis for each flow rate is based on a one-way ANOVA, followed by post hoc Tukey's pairwise comparisons. Asterisks denote statistically significant difference versus MB-cnt group, * $p < 0.05$, ** $p < 0.01$, *** $p < 0.001$. ANOVA: analysis of variance; SD: standard deviation; PBS: phosphate buffered saline; MB: microbubbles; MB-Prot: microbubbles functionalized with protamine; MNPh: magnetic nanoparticles coated with heparin.

We then began optimization of the microbubble's magnetic properties (Supplementary Material, Sections 1-2). Our theoretical analysis suggested that an estimated magnetic force threshold of 2×10^{-12} N would be required to capture a magnetic microsphere (~ 3 μm) at a characteristic capillary flow rate of solid tumors (~ 0.04 cm/s, Figure S1). The magnetic force exerted on a magnetic sphere depends on the magnetic moment of the sphere and the gradient of magnetic field. Considering a practically attainable magnetic field gradient of 50 T/m, we sought to prepare microbubbles with a magnetic moment of $>4 \times 10^{-14}$ Am². To tune the magnetic moment of microbubbles, we varied the loading of magnetic nanoparticles (MNPh) per microbubble. This could be achieved by varying the density of protamine on the microbubble's surface. Quantitative analysis revealed a positive linear correlation between

the extent of nanoparticle loading and the protamine surface density of MB-Prot ($R = 0.99$, $p = 0.002$, Figure 2, B). Microbubbles with nanoparticle loadings of 7 ± 1 fg/ μm^2 (MB-Prot/MNPh-s1), 11 ± 1 fg/ μm^2 (MB-Prot/MNPh-s2) and 17 ± 2 fg Fe/ μm^2 (MB-Prot/MNPh-s3) could be prepared using protamine surface densities of 0.22 ± 0.03 fg/ μm^2 , 0.32 ± 0.04 fg/ μm^2 and 0.42 ± 0.04 fg/ μm^2 , respectively. The microbubble sample MB-Prot/MNPh-s3 had an estimated magnetic moment of 4.3×10^{-14} Am², which fulfilled the theoretical magnetic capture requirement.

We tested the amenability of these microbubble samples to magnetic capture using a dynamic capture assay. Magnetic ($B = 0.9$ T, $\text{grad } B = 50$ T/m) capture of microbubbles was tested under physiologically relevant flow conditions using non-magnetic, protamine-free microbubbles (MB-cnt) as a control. At a tumor-mimicking flow rate of 0.04 cm/s, a major

fraction of MB-Prot/MNPh-s3 microbubbles ($82\pm 3\%$) was amenable to magnetic capture, while only a minor fraction of MB-Prot/MNPh-s2 and MB-Prot/MNPh-s1 could be captured under the same conditions (Figure 2, C). Notably, MB-Prot/MNPh-s3 could be captured to a significantly higher extent than the non-magnetic control microbubbles (MB-cnt) at flow rates of up to 3 cm/s (for 3 cm/s, MB-Prot/MNPh-s3: $23\pm 3\%$ vs. MB-cnt: $5\pm 3\%$, $p < 0.001$). These results suggested that MB-Prot/MNPh-s3 could be amenable to *in vivo* magnetic capture. The optimized MB-Prot/MNPh-s3 microbubble preparation was termed MagMB and used in all subsequent studies.

MagMB exhibited a narrow size distribution (Figure 3, A) with a mean volume-weighted diameter of $3.1\pm 1.4\ \mu\text{m}$, similar to Definity ($3.99\ \mu\text{m}$ [38]). The electronegative zeta potential of MagMB ($-19\pm 4\ \text{mV}$) confirmed that heparin was displayed on the microbubble surface. Microbubble characterization using bright-field phase contrast microscopy and transmission electron microscopy further corroborated the association of MNPh with the

microbubbles (Figure 3: B, C-I and C-II). CryoTEM micrographs also confirmed the attachment of the nanoparticles to the microbubble's surface (Figure 3: C-III and C-IV). Importantly, incubation of MagMB with fetal bovine serum (FBS 50%, 30 min) did not significantly affect their MNPh content compared to incubation with PBS (FBS: $16\pm 3\ \text{fg}/\mu\text{m}^2$ vs. PBS: $17\pm 2\ \text{fg}/\mu\text{m}^2$, $p = 0.07$, Figure 3,D). Stability of MagMB in the presence of serum suggested that they would be stable in plasma.

Optimized magnetic microbubbles (MagMB) display high sensitivity to acoustic stimuli and visibility to ultrasonography

To assess whether MagMB retained the microbubble's sensitivity to ultrasound, we tested MagMB for acoustic destructibility and echogenicity. Acoustic destructibility was tested *in vitro* (Figure 4, A1) by exposing MagMB to acoustic insonations (1 MHz, 0.22 MPa, 33 μs pulse duration and 3 kHz pulse repetition frequency) of varying durations (0-80 s). The profiles of acoustically-induced decay in particle

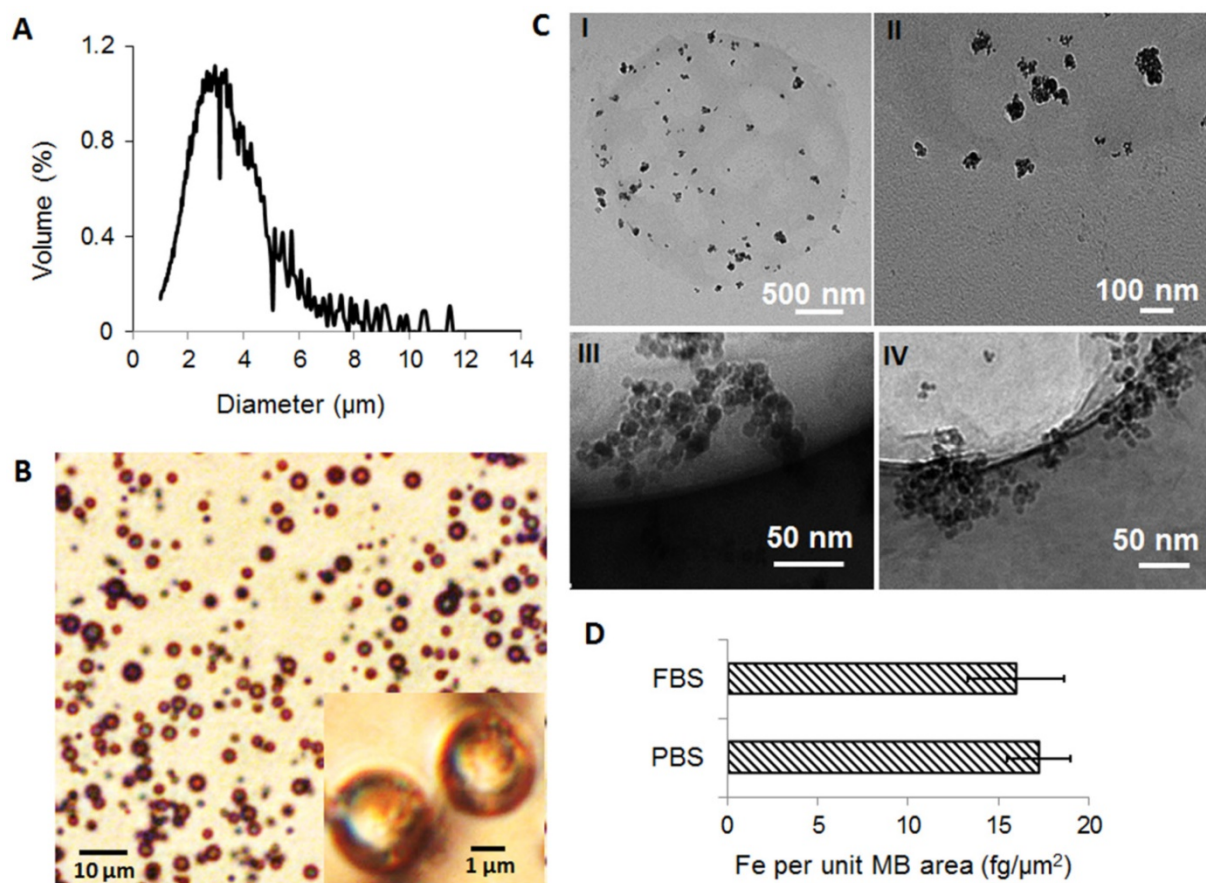


Figure 3. Characterization of the optimized magnetic microbubbles, MagMB. A. Representative volume-weighted size distribution of MagMB dispersed in PBS, pH 7.4. B. Representative bright-field phase contrast micrographs of MagMB; inset - representative high magnification (100x) phase-contrast micrograph of MagMB. C. Representative TEM (I and II) and cryoTEM (III and IV) micrographs of MagMB. Micrographs I and III illustrate the composition of microbubbles and the multi-core structure of the MNPh nanoparticles, respectively. Micrographs II and IV illustrate attachment of nanoparticles to the microbubble's surface. D. Analysis of MagMB stability in the presence of serum (50% FBS) as compared to PBS controls. Data represent mean \pm SD, $n = 4$. Statistical comparison is based on unpaired t test; $p = 0.07$. CryoTEM: cryogenic transmission electron microscopy; FBS: fetal bovine serum; MagMB: magnetic microbubbles; MB: microbubbles; MNPh: magnetic nanoparticles coated with heparin; PBS: phosphate buffered saline; SD: standard deviation; TEM: transmission electron microscopy.

counts for MagMB ($t_{1/2} = 18 \pm 3$ s) did not differ significantly ($p = 0.375$) from those recorded for the FDA-approved microbubbles, Definity ($t_{1/2} = 22 \pm 3$ s), or from the control, non-magnetic MB-cnt ($t_{1/2} = 16 \pm 4$ s) (Figure 4, A2). Previously reported formulations of magnetic microbubbles showed a significantly attenuated acoustic performance compared to

clinically used contrast agents, likely due to the stiffening of the microbubble shell [11]. Unlike previous formulations, MagMB displayed Definity-like acoustic sensitivity demonstrating that they retained the acoustic properties of the microbubble contrast agents optimized for acoustic performance.

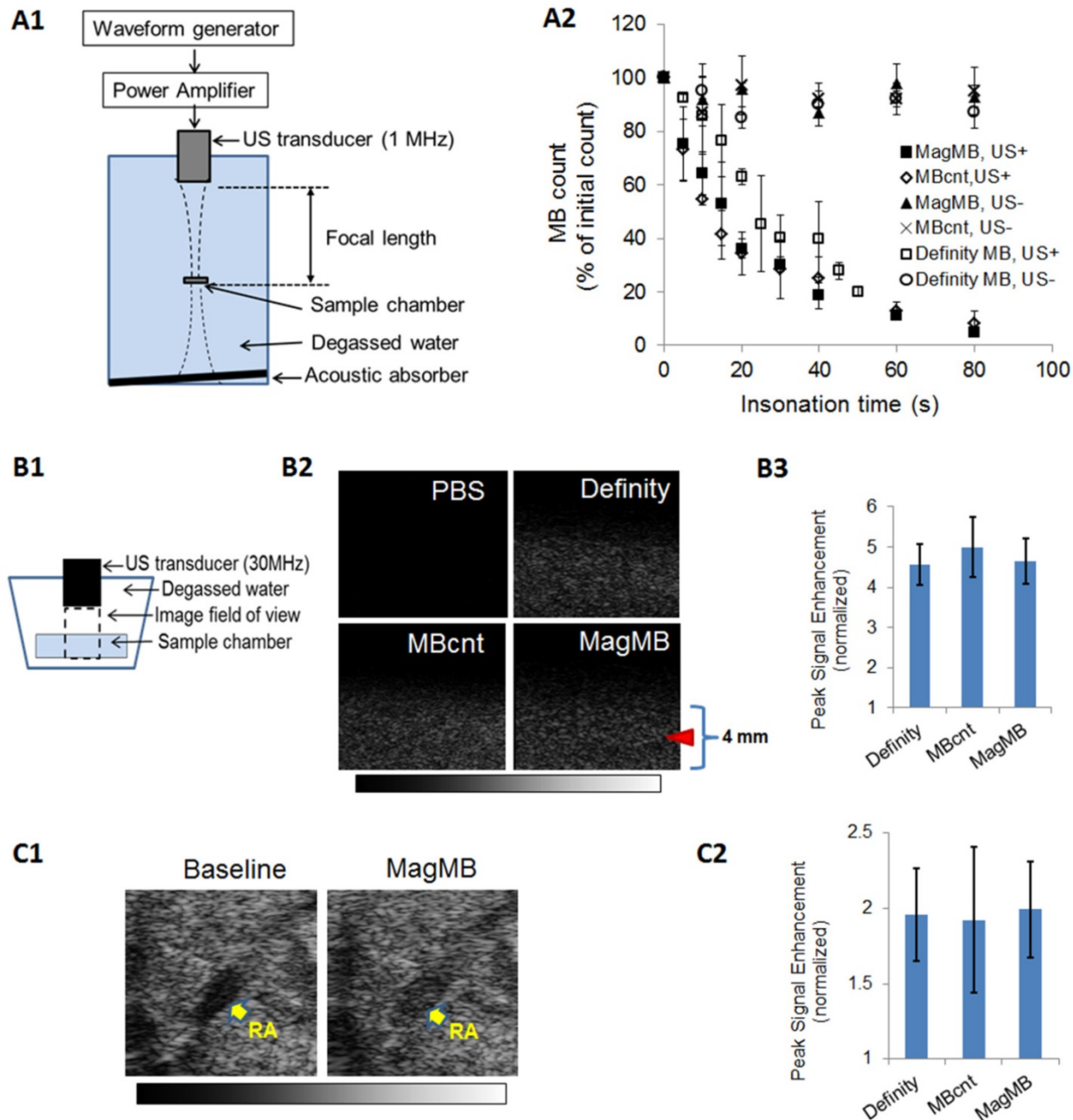


Figure 4. Analysis of acoustic properties of MagMB. (A1) *In vitro* setup for assessing acoustic destructibility of microbubbles (full description of the setup is provided in methods, section “Acoustic destructibility assay”). (A2) Amenability of microbubble suspensions (10^7 /mL) to destruction by ultrasound: ‘US+’ = 1 MHz tone-bursts of ultrasound insonation at 0.22 MPa peak negative pressure, 33 μ s pulse duration, 3 kHz pulse repetition frequency and 0-80 s exposure time; ‘US-’ = no ultrasound insonation. Data represent mean \pm SD, n = 4. (B1) *In vitro* setup for examining microbubble suspensions by B-mode ultrasonography. (B2) Representative B-mode ultrasonograms of MagMB, Definity and MBcnt suspensions in phosphate-buffered saline (10^6 /mL, PBS, pH 7.4); and a reference ultrasonogram of PBS solution. The images were acquired with a 30 MHz transducer at 20% transmit power and 40 dB gain. Arrow depicts focal depth. (B3) *In vitro* echogenicity of microbubbles measured as background-normalized signal enhancement of PBS solution. Data represent mean \pm SD, n = 4. (C1) Representative *in vivo* ultrasonograms demonstrating contrast enhancement of the renal artery by MagMB following i.v. bolus administration of the microbubbles (7.5×10^7 MB/kg, 100 μ L) as compared to the baseline acquired prior to microbubble injection. The images were acquired with a 30 MHz transducer at 20% transmit power and 20 dB gain. (C2) *In vivo* echogenicity of microbubbles measured as background-normalized peak signal enhancement of renal artery. Data represent mean \pm SD, n = 4. MB: microbubbles; PBS: phosphate buffered saline; RA: renal artery; SD: standard deviation; US: ultrasound.

We further compared the echogenicity of MagMB to that of Definity and MB-cnt using high-frequency (30 MHz) fundamental-mode ultrasonography. First, we examined B-mode ultrasonograms of microbubble suspensions *in vitro* (Figure 4, B1-B2). The *in vitro* echogenicity of MagMB (4.6 ± 0.6) did not differ significantly ($p = 0.68$) from that produced by MB-cnt (5.0 ± 0.7) or Definity (4.6 ± 0.6 ; Figure 4, B3). We next examined the echogenicity of MagMB *in vivo* by measuring contrast enhancement of renal artery after an i.v. bolus dose of microbubbles (7.5×10^7 MB/kg, Figure 4, C1). Similar to the *in vitro* results, the *in vivo* echogenicity of MagMB (2.0 ± 0.3) did not differ significantly ($p = 0.97$) from that produced by MB-cnt (1.9 ± 0.5) or Definity (1.9 ± 0.3 ; Figure 4, C2). Because echogenicity of lipid-shelled microbubbles is a manifestation of their compressibility, high Definity-like echogenicity of MagMB provided evidence that MagMB, unlike previously reported formulations, retained the original compressibility of “true” gaseous microbubbles coated with a phospholipid monolayer shell (such as Definity and MB-cnt) [6, 11].

The ability of lipid-shelled microbubbles (e.g., Definity) to evade lung entrapment and circulate systemically has been ascribed to their compressibility and surface protection by stealth coatings [5, 26]. A combination of properties displayed by the MagMB including compressibility, surface protection with stealth heparin and stability in serum suggested that MagMB may be able to emulate the *in vivo* behavior of the original lipid-shelled microbubbles and circulate systemically.

MagMB circulate systemically and evade entrapment in the lungs

To examine the *in vivo* performance of MagMB, we assessed their biodistribution and pharmacokinetics. To study biodistribution, we labeled MagMB with a near infrared dye Cy5.5 (MagMB-Cy5.5). At 30 min after i.v. bolus administration of MagMB-Cy5.5, the majority of Cy5.5 dose (68 ± 11 %dose/g tissue) was localized in the liver with a minor fraction found in the spleen (19 ± 10 %dose/g tissue, Figure 5, A1-A2). Importantly, the lungs were found to contain a very low fraction of the dose (7 ± 5 %dose/g tissue). This fraction corresponded to $\sim 1\%$ of the Cy5.5 dose per total mass of the lung tissue ($\sim 0.5\%$ per each lung) and was 17- to 90-fold lower than the fraction of the dose reported to be entrapped in the lungs with previous magnetic microbubble formulations [11, 14]. These findings suggested that, in contrast to previous formulations, MagMB could successfully evade entrapment in pulmonary capillaries.

We also explored whether an undesirable entrapment in the lungs could have occurred at earlier time points post administration. Previous studies demonstrated that composite microbubbles are initially entrapped in lung capillaries and then redistribute to the liver [14, 25]. To examine this possibility, we performed kinetic monitoring of the MagMB-Cy5.5 biodistribution using fluorescence imaging over the time interval of 2-30 min post-injection (Figure 5, C1-C2). At 2 min post injection, the lungs displayed negligible fluorescence, while the average fluorescence signal in the liver was a 1.5-fold higher than in the lungs. Over the subsequent time interval of 2-30 min post injection, the lungs showed no significant changes in fluorescent signal, ruling out the possibility of early lung entrapment followed by subsequent redistribution to the liver. In contrast, the liver exhibited a gradual increase in fluorescence over time that culminated in a plateau at 15 min post administration. These observations corroborated that the MagMB evaded lung entrapment and suggested that hepatic clearance was the main mechanism of MagMB elimination. The accumulation of MagMB in the liver displayed mono-exponential recovery kinetics with a half-life of 3.6 ± 0.9 min, suggesting that MagMB circulated systemically (Figure 5, C2).

We next evaluated the pharmacokinetics of MagMB. We used ultrasonography (30 MHz, fundamental mode) to monitor MagMB-induced contrast enhancement in the renal artery as a relative measure of MagMB concentrations in systemic circulation. Similar ultrasonographic procedures were previously utilized to assess the pharmacokinetics of echogenic microbubbles. [45] After an i.v. bolus dose of MagMB (1×10^9 /kg), signal enhancement of the renal artery could be detected for up to 13.3 ± 0.9 min post injection, revealing that MagMB persisted in systemic circulation (Figure 5, B1-B2). Elimination of MagMB exhibited a two-phase profile with an initial faster phase responsible for the majority of MagMB clearance ($>70\%$ of area-under-the-curve) and a slower terminal phase. The half-life of the initial elimination phase was 2.8 ± 0.8 min, which is comparable with the half-lives of clinically employed lipid-shelled microbubbles (Definity, 1.2-3 min) [45].

Circulating MagMB can be accumulated in tumors by magnetic targeting, monitored by ultrasonography and collapsed by ultrasound

To study the behavior of MagMB in tumors, we monitored MagMB transit through the tumor by ultrasonography (30 MHz, fundamental mode). The animals were positioned within the custom-assembled setup for magneto-acoustic targeting and

ultrasonography monitoring (Figure 6, A1-A3). The image field of view was aligned with the mid-plane tumor cross-section that passes through the geometrical center of the tumor (Figure 6, A4-A5).

We first examined the MagMB performance in control mice that were not subjected to external physical triggers (Figure 6, B – control). Following i.v. bolus administration of MagMB (1×10^9 /kg), the tumor ROI in control mice displayed a detectable signal enhancement at about 5-10 s post injection, reaching a peak value (7.7 ± 0.9 a.u.) at 1 min post injection (Figure 6, C:top panel, D:blue curve). This value corresponded to ~13% of the mean signal enhancement (at the peak) observed in the renal artery (60 ± 9 a.u.). Because the vascular space of subcutaneous tumor allografts in mice accounts for

~15% of the total tumor volume [46], these findings indicated vascular confinement of MagMB within the tumor and reflected perfusion of the tumor with echogenic MagMB. Following the peak at 1 min post-injection, the signal enhancement in the tumor ROI dissipated rapidly consistent with the rapid elimination of MagMB from systemic circulation. Similar tumor elimination profile was also observed by fluorescence imaging following administration of MagMB-Cy5.5 (Figure S4). The duration of signal enhancement in the tumor ROI did not significantly differ from the duration of signal enhancement in the renal artery ROI (15 ± 1 min vs. 13.3 ± 0.9 min, $p=0.09$) indicating that MagMB were not retained in tumors of control animals.

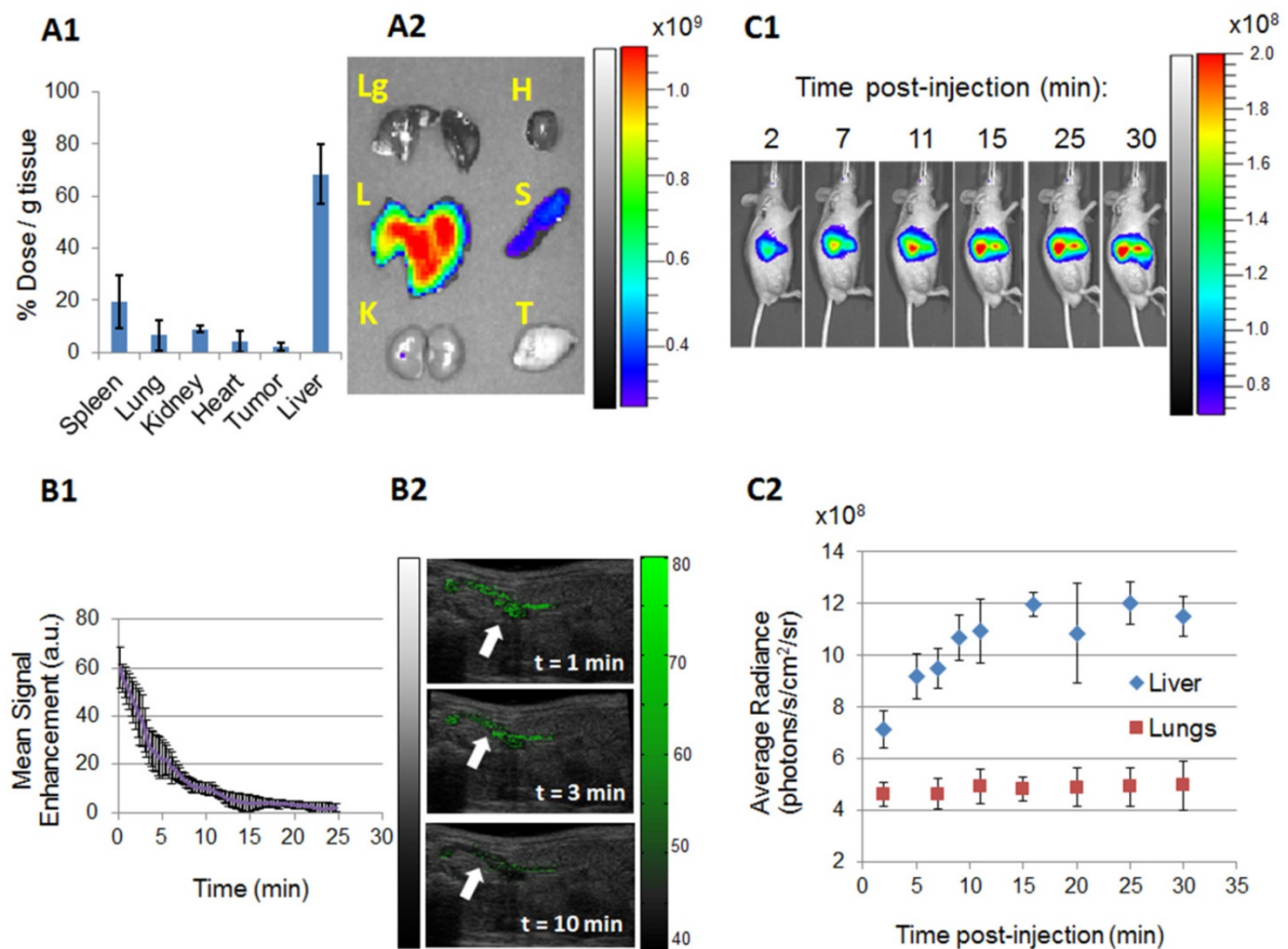


Figure 5. In vivo pharmacokinetics and biodistribution of MagMB. (A1) Organ biodistribution of MagMB-Cy5.5 quantified ex vivo by fluorescence spectrophotometry 30 min post administration. Data represent mean \pm SD, n = 4. (A2) Representative qualitative biodistribution profiles of MagMB-Cy5.5 analyzed by fluorescence imaging 30 min post-administration. Lg: lungs; L: liver; K: kidneys; H: heart; S: spleen; T: tumor. Color bar represents fluorescence radiant efficiency expressed in [photon/s/cm²/steradian]/[μ W/cm²]. (B1) Ultrasonography-based pharmacokinetics of MagMB, measured as mean contrast enhancement of renal artery over time (30 MHz, fundamental mode). Data represent mean \pm SD, n = 4. (B2) Representative ultrasonograms of renal artery at different time points after i.v. bolus injection of MagMB (1×10^9 /kg); images depict overlays of contrast-enhancement maps over anatomical B-mode scans. Renal artery is identified by white arrows. The color bar represents contrast enhancement in arbitrary units. A.u.: arbitrary units (C1) Representative kinetic sequence of the MagMB-Cy5.5 organ distribution analyzed by *in vivo* whole-body fluorescence imaging over a 30 min time interval post administration. The color bar represents fluorescence radiance expressed in [photon/s/cm²/steradian]. (C2) Average radiance sequentially analyzed for the liver and the lung ROIs over a 30 min time interval post MagMB-Cy5.5 administration. Data represent mean \pm SD, n = 4. ROI: region of interest; SD: standard deviation.

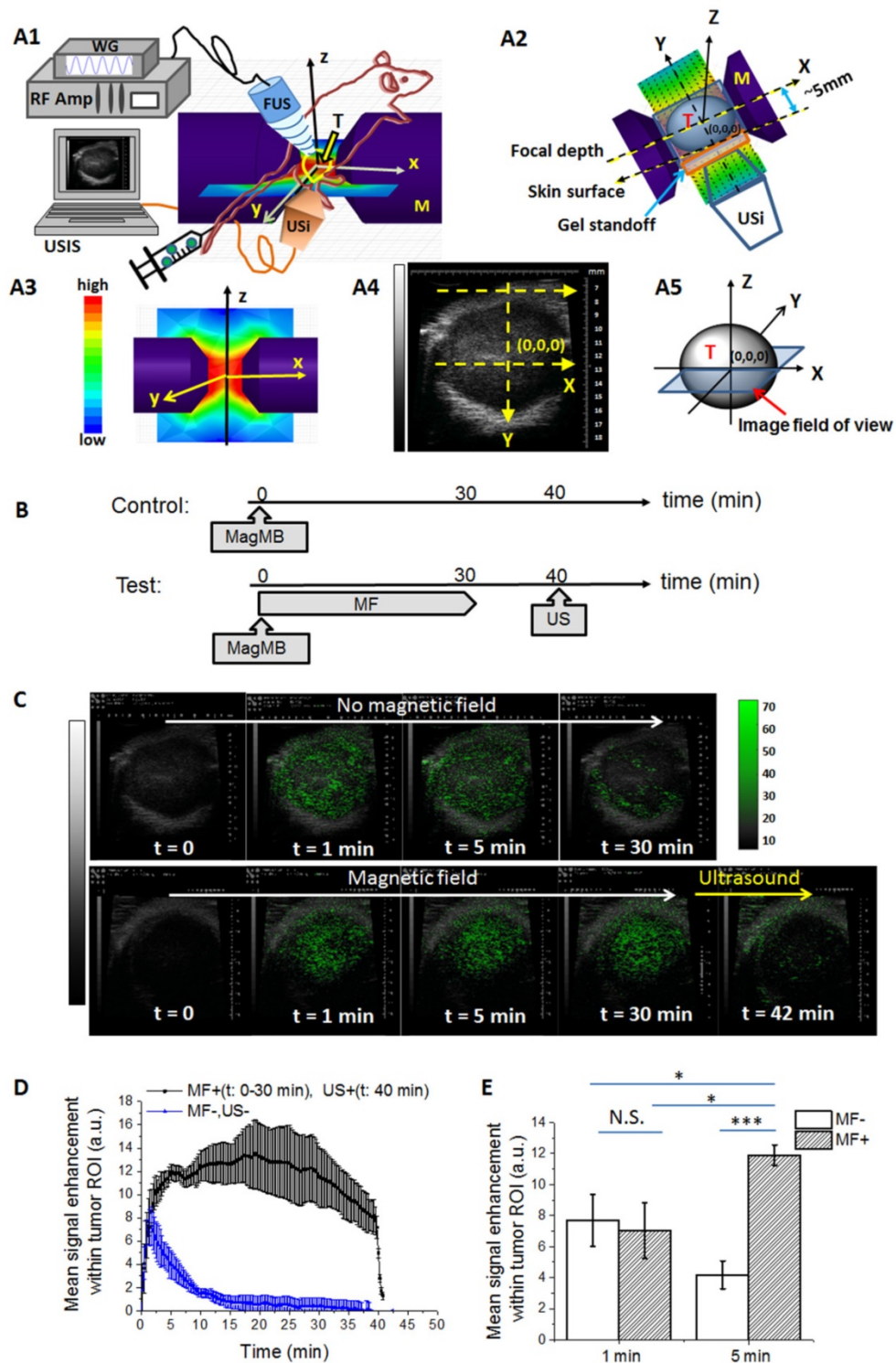


Figure 6. *In vivo* magneto-acoustic modulation of MagMB monitored by ultrasonography. (A1) Schematic depiction of the setup for magneto-acoustic tumor targeting and ultrasonographic monitoring. The flank tumor is positioned in the air-gap between the poles of a dipole electromagnet. The actuating ultrasound transducer (1 MHz) and the ultrasound imaging transducer (30 MHz) are aligned orthogonally along the z and y dimensions. The actuating transducer is driven by a wavefunction generator and a radio frequency amplifier. The images are acquired by an ultrasound imaging system. FUS: focused ultrasound; M: magnet; RF amp: radio frequency amplifier; T: tumor; US: ultrasound; USi: ultrasound imaging; USIS: ultrasound imaging system; WG: wavefunction generator. (A2) Top view of the setup: demonstrates the tumor positioning within the magnet and the alignment of the imaging probe relative to the tumor and the magnetic field. The coordinates (0,0,0) represent the geometrical tumor center. (A3) Magnetic field topography generated by the dipole electromagnet. (A4) Representative ultrasonogram of the tumor cross-section acquired using the probe alignment depicted in A2. (A5) Schematic depiction of the image field of view: image field of view is aligned with the mid-plane tumor cross-section that passes through the geometrical tumor center (0,0,0). (B) Time-line of the magnetic targeting and ultrasound treatments following MagMB administration. MagMB: magnetic microbubbles; MF: magnetic field; US: ultrasound. (C) Representative ultrasonograms of the tumor at different time points after i.v. bolus injection of MagMB (1×10^9 /kg) without (top panel, MF-, US-) and with (bottom panel) application of magnetic field (MF+: t = 0-30 min, 0.9 T, 50 T/m) and ultrasound (US+: t = 40 min, 1 MHz, PNP = 0.22 MPa, PD = 33 μ s, PRF = 3 kHz, exposure time = 50 s). Images depict overlays of contrast-enhancement maps over anatomical B-mode scans. The color bar represents contrast enhancement in arbitrary units. A.u.: arbitrary units; PD: pulse duration; PNP: peak negative pressure; PRF: pulse repetition frequency. (D) Kinetics of MagMB transit through the tumor without (blue) and with (black) application of magnetic field (MF+: t = 0-30 min, 0.9 T, 50 T/m) and ultrasound (US+: t = 40 min, 1 MHz, PNP = 0.22 MPa, PD = 33 μ s, PRF = 3 kHz, exposure time = 50 s). Data represents mean contrast enhancement within the tumor ROI in arbitrary units; mean \pm SD, n = 4. (E) Comparison of mean contrast enhancement within the tumor ROI at 1 min and 5 min post-administration of MagMB with (MF+) and without (MF-) application of magnetic field. Statistical analysis is based on a one-way ANOVA, followed by post hoc Tukey's pairwise comparisons. Asterisks denote statistically significant differences, *p < 0.05, **p < 0.01, ***p < 0.001, N.S.: p > 0.05. ANOVA: analysis of variance; N.S.: not significant; ROI: region of interest; SD: standard deviation.

We next asked whether MagMB could be amenable to magnetic targeting. Application of magnetic field ($B = 0.9$ T, $\text{grad } B = 50$ T/m) to tumor lesions of mice after i.v. bolus of MagMB (1×10^9 /kg) significantly altered the kinetics and the magnitude of ultrasonographic signal enhancement compared to controls (Figure 6, C: bottom panel, D: black curve). Following the initial wash-in phase, the signal in the tumor ROI of magnetically targeted animals displayed a gradual increase and reached a plateau at 5 min post injection. This plateau-level contrast enhancement persisted for the entire duration of magnetic targeting (up to 30 min). Overall, the signal enhancement in magnetically targeted animals reached a significantly higher magnitude than in controls (11.8 ± 0.6 a.u. vs. 7.7 ± 0.9 a.u., $p = 0.02$) and exhibited a significantly longer duration than in controls (30 ± 2 min vs. 15 ± 1 min, $p < 0.001$). Notably, at 30 min post injection, the signal enhancement in magnetically targeted animals was 15-fold higher than in controls (12 ± 2 a.u. vs. 0.7 ± 0.8 a.u., $p = 0.03$). These findings demonstrated that MagMB could be magnetically accumulated and retained in the tumor.

We also asked whether the magnetically captured MagMB retained their amenability to acoustic collapse. We exposed the tumors of magnetically targeted animals to ultrasound. A brief (50 s, ~ 3 half-lives) acoustic exposure (1 MHz, PNP = 0.22 MPa, PD = 33 μ s, PRF = 3 kHz) was sufficient to collapse magnetically captured MagMB, as reflected by a rapid signal decay within the tumor ROI (Figure 6, C: bottom panel, D: black curve $t > 40$ min). This result indicated that magnetically captured microbubbles indeed retained their acoustic sensitivity, and were amenable to both the magnetic and the acoustic modulation *in vivo*.

Drug delivery to tumors using MagMB can be enhanced by adjusting the magneto-acoustic targeting based on real-time monitoring of MagMB by ultrasonography

We evaluated the potential of MagMB to improve drug delivery to tumors. We assessed delivery of a model drug Cy5.5 using MagMB-Cy5.5 as a delivery platform and evaluated the feasibility of modulating delivery by a combination of magnetic targeting and ultrasound (Figure 7). Ultrasound-triggered microbubble destruction (UTMD) has been extensively investigated as a drug-targeting mechanism because of its ability to simultaneously release the microbubble-loaded drug and promote its access to tissue parenchyma of the target tissue [5, 8]. However, low efficiency of this mechanism limits its translational potential. Previous work demonstrated that the UTMD efficiency can be increased by

increasing local microbubble concentration at the target site with local microbubble injections [47]. We asked whether concentrating the MagMB-Cy5.5 in tumor vasculature by magnetic targeting prior to applying UTMD could similarly improve the drug delivery efficiency with systemic microbubble administration.

First, we subjected mice to a combination of magnetic targeting and UTMD (magneto-acoustic targeting), applying magnetic targeting for 1 min (Figure 7, A). The level of tumor fluorescence in mice achieved with this procedure (at 120 min post treatment) did not differ significantly from the levels achieved with the UTMD alone (Figure 7B-C, $2.6 \pm 0.4 \times 10^8$ photon/s vs. $2.5 \pm 0.3 \times 10^8$ photon/s, $p = 0.91$). These results suggested that 1 min duration of magnetic targeting may have not been sufficient to concentrate MagMB in tumor vasculature. This result was consistent with the ultrasonography observations, which revealed that application of magnetic targeting for 1 min did not significantly enhance the accumulation of MagMB in tumor vasculature compared to controls not subjected to magnetic targeting (Figure 6D, 7 ± 2 a.u. vs. 8 ± 2 a.u., $p = 0.92$).

Ultrasonographic monitoring of MagMB suggested that MagMB accumulation in the tumor by magnetic targeting occurs gradually over time (Figure 6D). We asked whether real-time ultrasonographic information on kinetics of the MagMB accumulation in the tumor could be leveraged to optimize drug delivery. Based on ultrasonographic monitoring, MagMB could be concentrated in the tumor to a significantly higher extent by 5 min of magnetic targeting than by 1 min of magnetic targeting (Figure 6D-E, 11.8 ± 0.6 a.u. vs. 7 ± 2 a.u., $p = 0.01$). We therefore explored the effect of magneto-acoustic targeting on drug delivery when applying magnetic targeting for 5 min. Indeed, with 5 min of magnetic targeting, a 2-fold higher tumor fluorescence was observed in magneto-acoustically targeted mice than in mice subjected to the UTMD alone (Figure 7B-C, $4.1 \pm 0.4 \times 10^8$ photon/s vs. $1.9 \pm 0.3 \times 10^8$ photon/s, $p < 0.01$). These results revealed that combining UTMD with magnetic targeting can indeed enhance the drug targeting efficiency by UTMD, provided that magnetic targeting is applied for sufficient time to concentrate the MagMB in tumor vasculature. Importantly, these findings also demonstrated that non-invasive ultrasonography could provide the required kinetic information on MagMB accumulation in the tumor, allowing real-time adjustment of the magnetic targeting and UTMD to enhance drug delivery.

Notably, although MagMB could be accumulated in the tumor by magnetic targeting alone, as evident from the ultrasonography results

(with 5 min of magnetic targeting), Cy5.5 delivery to tumors with magnetic targeting alone did not differ significantly from non-targeted controls (Figure 7B-C, $0.5 \pm 0.4 \times 10^8$ photon/s vs. $0.1 \pm 0.2 \times 10^8$ photon/s, $p=0.72$). While ultrasonographic monitoring of MagMB accumulation in the tumor by magnetic targeting was carried out in real-time, the fluorescence measurements of drug delivery were performed 120 min post treatment (Figure 7A). Thus, the apparent discrepancy is likely attributed to the reversal of magnetic holding of MagMB-Cy5.5 with the removal of the magnetic field. Similar reversal of magnetic carrier entrapment with the removal of the magnetic field has been reported in previous studies. [34] Our ultrasonography results demonstrating the decay of ultrasonographic contrast enhancement by magnetically-entrapped MagMB following removal of

magnetic field are consistent with this behavior (Figure 6D, time interval $30 < t < 40$ min). In contrast to magnetic targeting alone, the UTMD component of the combined magneto-acoustic targeting has likely promoted the extravasation of the released drug Cy5.5 into the tumor parenchyma, prolonging its residence within the tumor. Mechanical forces associated with microbubble collapse by ultrasound (e.g., shock waves, sonic jets) have been shown to increase permeability of the vascular barrier and propel drug-containing fragments of the microbubble's shell into the tissue parenchyma. [8, 48, 49] Similar phenomena are likely responsible for the prolonged residence of Cy5.5 in tumors exposed to the UTMD in our studies, but further work is required to elucidate the mechanism.

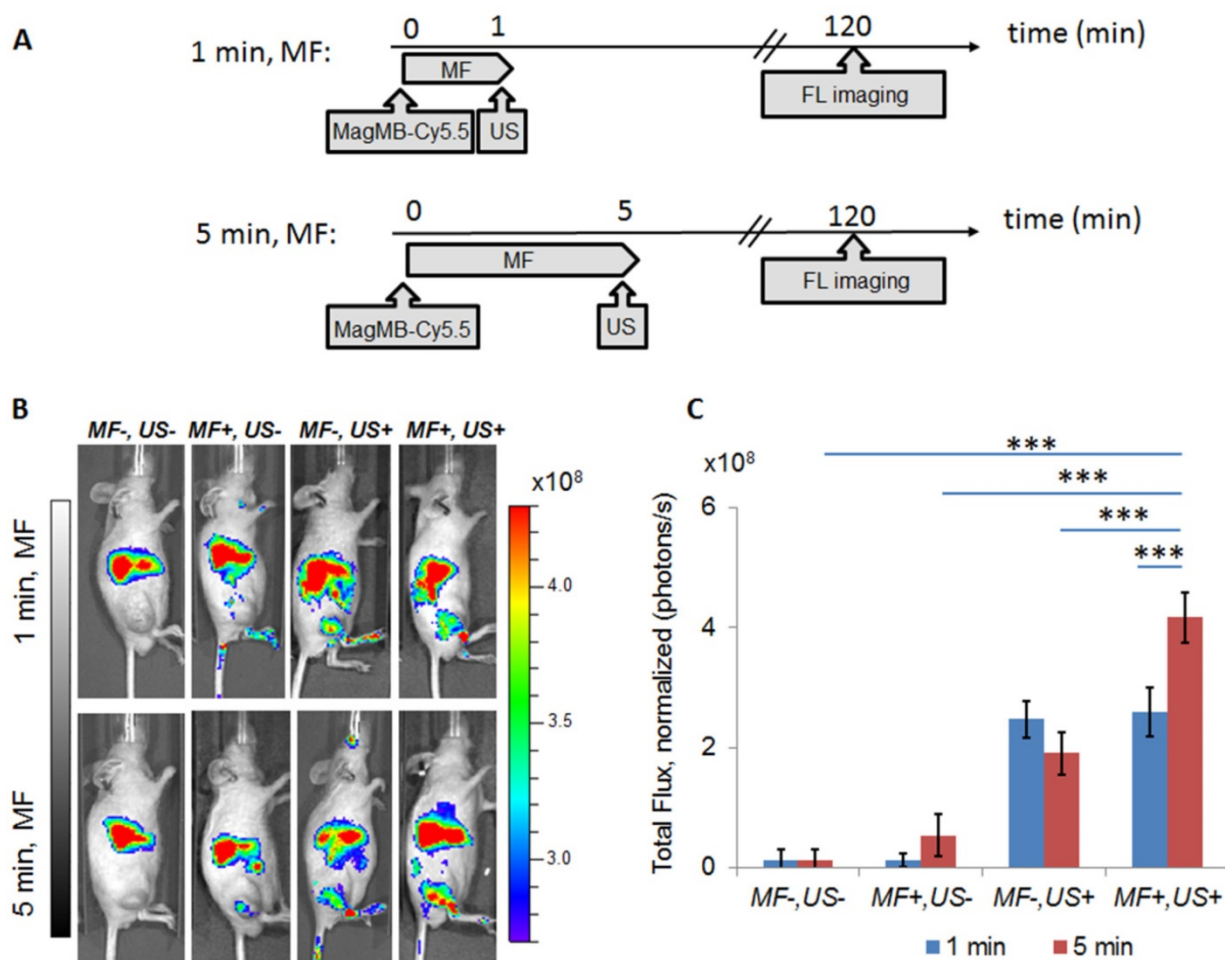


Figure 7. *In vivo* delivery of a model drug Cy5.5 to tumors using MagMB-Cy5.5 and magneto-acoustic modulation. (A) Time-line of the magnetic targeting and ultrasound treatments following MagMB-Cy5.5 administration and the subsequent drug delivery evaluation by fluorescence imaging. FL: fluorescence; MagMB: magnetic microbubbles; MF: magnetic field; US: ultrasound. (B) Representative qualitative biodistribution profiles of Cy5.5 analyzed by fluorescence imaging 120 min post administration of MagMB-Cy5.5 under different modulation conditions: (MF-, US-) no magnetic targeting or ultrasound, (MF+, US-) magnetic targeting only, (MF-, US+) ultrasound only, (MF+, US+) combination of magnetic targeting and ultrasound. Magnetic targeting (MF+: 0.9 T, 50 T/m) was applied for 1 min (top row) or 5 min (bottom row), immediately followed by ultrasound (US+: 1 MHz, PNP = 0.22 MPa, PD = 33 μ s, PRF = 3 kHz) for 50 s. MF: magnetic field; PD: pulse duration; PNP: peak negative pressure; PRF: pulse repetition frequency; US: ultrasound. Color bar represents fluorescence radiant efficiency expressed in [photon/s/cm²/steradian]/[μ W/cm²]. (C) Comparison of total fluorescence flux within the tumor ROI (photon/s) achieved under experimental conditions in B. The fluorescence flux of test animals in all groups was background corrected by subtracting the tumor ROI flux of blank controls – animals not exposed to MagMB-Cy5.5. Data represent mean \pm SD, $n = 4$. Statistical analysis is based on a one-way ANOVA, followed by post hoc Tukey's pairwise comparisons. Asterisks denote statistically significant differences: * $p < 0.05$, ** $p < 0.01$, *** $p < 0.001$. ANOVA: analysis of variance; ROI: region of interest; SD: standard deviation.

Conclusions

Taken together, we demonstrate the feasibility of leveraging magnetic microbubbles to enhance drug delivery to tumors by first magnetically concentrating these agents in tumor vasculature and then applying ultrasound to facilitate microbubble collapse. To realize this paradigm, we developed circulating magnetic microbubbles (MagMB) that exhibit strong magnetic and acoustic activities while also preserving circulation stability. Unlike previously reported magnetic microbubbles, MagMB evaded lung entrapment and could circulate systemically, which is likely due to the preserved compressibility of their lipid shell and surface protection with stealth heparin. We demonstrate that MagMB could reach tumor vasculature after systemic administration, allowing their modulation with magnetic and acoustic forcefields selectively in target tumors. Ultrasonographic monitoring of MagMB in tumor vasculature provided real-time information on the extent of microbubble accumulation by magnetic targeting and could be leveraged to time magnetic and ultrasonic actuation components for achieving drug delivery enhancement. MagMB could potentially be leveraged as a carrier for a wide variety of small molecule drugs. For example, for application in cancer therapy the therapeutic cargo could comprise chemotherapeutic drugs, sonosensitizers or immunomodulating agents. [40, 50-52] Overall, magnetic microbubbles (MagMB) in conjunction with ultrasound-guided magneto-acoustic modulation may provide a strategy for tailored minimally invasive control over delivery of therapeutic molecules to tumors and other target tissues. This approach warrants further investigation for development of tailored therapeutic strategies with improved efficacy and safety.

Abbreviations

DSPC: 1,2-distearoyl-*sn*-glycero-3-phosphocholine; DSPE-mPEG(2kDa): 1,2-distearoyl-*sn*-glycero-3-phosphoethanolamine-N-[methoxy(polyethylene glycol)-2000]; DSPE-PEG(2kDa)-MAL: 1,2-distearoyl-*sn*-glycero-3-phosphoethanolamine-N [maleimide(polyethylene glycol)-2000]; SPDP: N-Succinimidyl 3-[2-pyridyldithio]-propionate; DMSO: dimethyl sulfoxide; TCEP-HCL: Tris(2-carboxyethyl) phosphine hydrochloride; MALDI-TOF MS: matrix assisted laser desorption/ionization-time of flight mass spectrometry; BCA: bicinchoninic acid; ICP-OES: inductively coupled plasma optical emission spectrometry; TEM: transmission electron microscopy; cryoTEM: cryogenic transmission electron microscopy; PD: pulse duration; PRF: pulse

repetition frequency; PNP: peak negative pressure; PBS: phosphate buffered saline; FBS: fetal bovine serum; LL/2: Lewis lung carcinoma; EDTA: ethylenediaminetetraacetic acid; DC: direct current; UTMD: ultrasound targeted microbubbles destruction; MF: magnetic field; US: ultrasound; FUS: focused ultrasound; USi: ultrasound imaging; WG: wavefunction generator; M: magnet; RF amp: radio frequency amplifier; CE: contrast enhancement; ROI: region of interest; RA: renal artery; T: tumor; ANOVA: analysis of variance; SD: standard deviation; MNPh: magnetic nanoparticles coated with heparin; MB: microbubbles; MB-Prot: microbubbles functionalized with protamine; MagMB: magnetic microbubbles; PL: phospholipid; PEG: poly(ethylene glycol); Prot: protamine; FL: fluorescence.

Supplementary Material

Supplementary methods sections 1-2, figures S1-S4 and table S1: theoretical analysis of magnetic capture requirements, estimation of microbubble's magnetic moment, representative microbubble size distributions and counts during purification steps, monitoring of microbubble transit through tumor vasculature by fluorescence imaging.
<http://www.thno.org/v08p0341s1.pdf>

Acknowledgements

We thank G.L. Amidon for critical feedback on the manuscript, D.G. Anderson, C. G. Levins and C. Kastrup for constructive discussions, C. Bergemann for the generous gift of iron oxide nanoparticles, L. Thapa for assistance with processing animal tissues and J. Mitchell for editing this manuscript. This work was supported by the National Institute of Health, Centers for Cancer Nanotechnology Excellence (U54 CA151884 to RL), the St. Baldrick's Foundation Career Development Award (354400 to BC), the Brain Research Foundation Fay/Frank Seed Grant (BRFSG-2015-09 to BC) and the William and Sally Seale Fund for Cancer Research (to BC).

Competing Interests

The authors have declared that no competing interest exists.

References

- Bae YH, Park K. Targeted drug delivery to tumors: myths, reality and possibility. *J Control Release*. 2011; 153: 198-205.
- Mura S, Nicolas J, Couvreur P. Stimuli-responsive nanocarriers for drug delivery. *Nat Mater*. 2013; 12: 991-1003.
- Pene F, Courtine E, Cariou A, Mira JP. Toward theragnostics. *Crit Care Med*. 2009; 37: S50-8.
- Jeelani S, Reddy RC, Maheswaran T, Asokan GS, Dany A, Anand B. Theragnostics: A treasured tailor for tomorrow. *J Pharm Bioallied Sci*. 2014; 6: S6-8.
- Ferrara KW, Borden MA, Zhang H. Lipid-shelled vehicles: engineering for ultrasound molecular imaging and drug delivery. *Acc Chem Res*. 2009; 42: 881-92.

6. Sirsi S, Borden M. Microbubble Compositions, Properties and Biomedical Applications. *Bubble Sci Eng Technol*. 2009; 1: 3-17.
7. Owen J, Pankhurst Q, Stride E. Magnetic targeting and ultrasound mediated drug delivery: benefits, limitations and combination. *Int J Hyperthermia*. 2012; 28: 362-73.
8. Ferrara K, Pollard R, Borden M. Ultrasound microbubble contrast agents: fundamentals and application to gene and drug delivery. *Annu Rev Biomed Eng*. 2007; 9: 415-47.
9. Chen CC, Sirsi SR, Homma S, Borden MA. Effect of surface architecture on in vivo ultrasound contrast persistence of targeted size-selected microbubbles. *Ultrasound Med Biol*. 2012; 38: 492-503.
10. Cai X, Yang F, Gu N. Applications of magnetic microbubbles for theranostics. *Theranostics*. 2012; 2: 103-12.
11. Vlaskou D, Mykhaylyk O, Krotz F, Hellwig N, Renner R, Schillinger U, et al. Magnetic and Acoustically Active Lipospheres for Magnetically Targeted Nucleic Acid Delivery. *Adv Funct Mater*. 2010; 20: 3881-94.
12. Owen J, Zhou B, Rademeyer P, Tang MX, Pankhurst Q, Eckersley R, et al. Understanding the structure and mechanism of formation of a new magnetic microbubble formulation. *Theranostics*. 2012; 2: 1127-39.
13. Sciallero C, Balbi L, Paradossi G, Trucco A. Magnetic resonance and ultrasound contrast imaging of polymer-shelled microbubbles loaded with iron oxide nanoparticles. *R Soc Open Sci*. 2016; 3: 160063.
14. Barrefelt AA, Brismar TB, Egri G, Aspelin P, Olsson A, Oddo L, et al. Multimodality imaging using SPECT/CT and MRI and ligand functionalized ^{99m}Tc-labeled magnetic microbubbles. *EJNMMI Res*. 2013; 3: 12.
15. Yang F, Li Y, Chen Z, Zhang Y, Wu J, Gu N. Superparamagnetic iron oxide nanoparticle-embedded encapsulated microbubbles as dual contrast agents of magnetic resonance and ultrasound imaging. *Biomaterials*. 2009; 30: 3882-90.
16. Liu Z, Lammers T, Ehling J, Fokong S, Bornemann J, Kiessling F, et al. Iron oxide nanoparticle-containing microbubble composites as contrast agents for MR and ultrasound dual-modality imaging. *Biomaterials*. 2011; 32: 6155-63.
17. Wu J, Leong-Poi H, Bin J, Yang L, Liao Y, Liu Y, et al. Efficacy of contrast-enhanced US and magnetic microbubbles targeted to vascular cell adhesion molecule-1 for molecular imaging of atherosclerosis. *Radiology*. 2011; 260: 463-71.
18. Crake C, Owen J, Smart S, Coviello C, Coussios CC, Carlisle R, et al. Enhancement and Passive Acoustic Mapping of Cavitation from Fluorescently Tagged Magnetic Resonance-Visible Magnetic Microbubbles in Vivo. *Ultrasound Med Biol*. 2016; 42: 3022-36.
19. Mannell H, Pircher J, Fochler F, Stampnik Y, Rathel T, Gleich B, et al. Site directed vascular gene delivery in vivo by ultrasonic destruction of magnetic nanoparticle coated microbubbles. *Nanomedicine*. 2012; 8: 1309-18.
20. Sciallero C, Grishenkov D, Kothapalli SV, Oddo L, Trucco A. Acoustic characterization and contrast imaging of microbubbles encapsulated by polymeric shells coated or filled with magnetic nanoparticles. *J Acoust Soc Am*. 2013; 134: 3918-30.
21. Chen CC, Borden MA. The role of poly(ethylene glycol) brush architecture in complement activation on targeted microbubble surfaces. *Biomaterials*. 2011; 32: 6579-87.
22. Merkel TJ, Jones SW, Herlihy KP, Kersey FR, Shields AR, Napier M, et al. Using mechanobiological mimicry of red blood cells to extend circulation times of hydrogel microparticles. *Proc Natl Acad Sci U S A*. 2011; 108: 586-91.
23. Fisher NG, Christiansen JP, Klibanov A, Taylor RP, Kaul S, Lindner JR. Influence of microbubble surface charge on capillary transit and myocardial contrast enhancement. *J Am Coll Cardiol*. 2002; 40: 811-9.
24. Warram JM, Sorace AG, Mahoney M, Samuel S, Harbin B, Joshi M, et al. Biodistribution of P-selectin targeted microbubbles. *J Drug Target*. 2014; 22: 387-94.
25. Barrefelt A, Saghafian M, Kuiper R, Ye F, Egri G, Klickermann M, et al. Biodistribution, kinetics, and biological fate of SPION microbubbles in the rat. *Int J Nanomedicine*. 2013; 8: 3241-54.
26. Lindner JR, Song J, Jayaweera AR, Sklenar J, Kaul S. Microvascular rheology of Definity microbubbles after intra-arterial and intravenous administration. *J Am Soc Echocardiogr*. 2002; 15: 396-403.
27. Stapleton S, Goodman H, Zhou YQ, Cherin E, Henkelman RM, Burns PN, et al. Acoustic and kinetic behaviour of definity in mice exposed to high frequency ultrasound. *Ultrasound Med Biol*. 2009; 35: 296-307.
28. Nguyen PN, Nikolova G, Polavarapu P, Waton G, Phuoc LT, Pourroy G, et al. Compressible multi-scale magnetic constructs: decorating the outer surface of self-assembled microbubbles with iron oxide nanoparticles. *RSC Adv*. 2013; 3: 7743-6.
29. Socha M, Bartecki P, Passirani C, Sapin A, Damge C, Lecompte T, et al. Stealth nanoparticles coated with heparin as peptide or protein carriers. *J Drug Target*. 2009; 17: 575-85.
30. Ramamurthy N, Baliga N, Wakefield TW, Andrews PC, Yang VC, Meyerhoff ME. Determination of low-molecular-weight heparins and their binding to protamine and a protamine analog using polyion-sensitive membrane electrodes. *Anal Biochem*. 1999; 266: 116-24.
31. Carlsson J, Drevin H, Axen R. Protein thiolation and reversible protein-protein conjugation. N-Succinimidyl 3-(2-pyridyldithio)propionate, a new heterobifunctional reagent. *Biochem J*. 1978; 173: 723-37.
32. Chertok B, Langer R, Anderson DG. Spatial Control of Gene Expression by Nanocarriers Using Heparin Masking and Ultrasound-Targeted Microbubble Destruction. *ACS Nano*. 2016; 10: 7267-78.
33. Kim DH, Costello MJ, Duncan PB, Needham D. Mechanical properties and microstructure of polycrystalline phospholipid monolayer shells: Novel solid microparticles. *Langmuir*. 2003; 19: 8455-66.
34. Chertok B, Moffat BA, David AE, Yu F, Bergemann C, Ross BD, et al. Iron oxide nanoparticles as a drug delivery vehicle for MRI monitored magnetic targeting of brain tumors. *Biomaterials*. 2008; 29: 487-96.
35. Chertok B, David AE, Yang VC. Magnetically-enabled and MR-monitored selective brain tumor protein delivery in rats via magnetic nanocarriers. *Biomaterials*. 2011; 32: 6245-53.
36. Chertok B, David AE, Huang Y, Yang VC. Glioma selectivity of magnetically targeted nanoparticles: a role of abnormal tumor hydrodynamics. *J Control Release*. 2007; 122: 315-23.
37. Feshitan JA, Chen CC, Kwan JJ, Borden MA. Microbubble size isolation by differential centrifugation. *J Colloid Interface Sci*. 2009; 329: 316-24.
38. Goertz DE, de Jong N, van der Steen AF. Attenuation and size distribution measurements of Definity and manipulated Definity populations. *Ultrasound Med Biol*. 2007; 33: 1376-88.
39. Karshafian R, Bevan PD, Williams R, Samac S, Burns PN. Sonoporation by Ultrasound-Activated Microbubble Contrast Agents: Effect of Acoustic Exposure Parameters on Cell Membrane Permeability and Cell Viability. *Ultrasound Med Biol*. 2009; 35: 847-60.
40. Wood AKW, Sehgal CM. A Review of Low-Intensity Ultrasound for Cancer Therapy. *Ultrasound Med Biol*. 2015; 41: 905-28.
41. Sorace AG, Warram JM, Umphrey H, Hoyt K. Microbubble-mediated ultrasonic techniques for improved chemotherapeutic delivery in cancer. *J Drug Target*. 2012; 20: 43-54.
42. Li P, Zheng Y, Ran H, Tan J, Lin Y, Zhang Q, et al. Ultrasound triggered drug release from 10-hydroxycamptothecin-loaded phospholipid microbubbles for targeted tumor therapy in mice. *J Control Release*. 2012; 162: 349-54.
43. Sirsi S, Feshitan J, Kwan J, Homma S, Borden M. Effect of Microbubble Size on Fundamental Mode High Frequency Ultrasound Imaging in Mice. *Ultrasound Med Biol*. 2010; 36: 935-48.
44. Sirsi SR, Hernandez SL, Zielinski L, Blomback H, Koubaa A, Synder M, et al. Polyplex-microbubble hybrids for ultrasound-guided plasmid DNA delivery to solid tumors. *J Control Release*. 2012; 157: 224-34.
45. Wu H, Roguin NG, Krupka TM, Solorio L, Yoshiara H, Guenette G, et al. Acoustic characterization and pharmacokinetic analyses of new nanobubble ultrasound contrast agents. *Ultrasound Med Biol*. 2013; 39: 2137-46.
46. Opitz AW, Wickstrom E, Thakur ML, Wagner NJ. Physiologically based pharmacokinetics of molecular imaging nanoparticles for mRNA detection determined in tumor-bearing mice. *Oligonucleotides*. 2010; 20: 117-25.
47. Song S, Shen Z, Chen L, Brayman AA, Miao CH. Explorations of high-intensity therapeutic ultrasound and microbubble-mediated gene delivery in mouse liver. *Gene Ther*. 2011; 18: 1006-14.
48. Huynh E, Rajora MA, Zheng G. Multimodal micro, nano, and size conversion ultrasound agents for imaging and therapy. *Wiley Interdiscip Rev Nanomed Nanobiotechnol*. 2016; 8: 796-813.
49. Pitt WG, Hussein GA, Staples BJ. Ultrasonic drug delivery--a general review. *Expert Opin Drug Deliv*. 2004; 1: 37-56.
50. Tinkov S, Coester C, Serba S, Geis NA, Katus HA, Winter G, et al. New doxorubicin-loaded phospholipid microbubbles for targeted tumor therapy: in-vivo characterization. *J Control Release*. 2010; 148: 368-72.
51. Adams JL, Smothers J, Srinivasan R, Hoos A. Big opportunities for small molecules in immuno-oncology. *Nat Rev Drug Discov*. 2015; 14: 603-22.
52. Kuroki M, Hachimine K, Abe H, Shibaguchi H, Kuroki M, Maekawa S, et al. Sonodynamic therapy of cancer using novel sonosensitizers. *Anticancer Res*. 2007; 27: 3673-7.